

Deposition of nano-hydroxyapatite particles utilising direct and transitional electrohydrodynamic processes

Z. Ahmad · E. S. Thian · J. Huang · M. J. Edirisinghe · S. M. Best ·
S. N. Jayasinghe · W. Bonfield · R. A. Brooks · N. Rushton

Received: 22 January 2008 / Accepted: 11 March 2008 / Published online: 5 April 2008
© Springer Science+Business Media, LLC 2008

Abstract Electrohydrodynamic spraying is a well established process used to deposit, coat, analyse and synthesise materials within the biomedical remit. Recently, electrohydrodynamic printing has been developed to afford structures for potential applications in the biomedical and medical engineering fields. Both of these processes rely on the formation of an electrically-induced jet, however the resulting products can be made strikingly different and offer potential in broader applications. Here we show how spraying and printing are linked by elucidating the ease of transition between the processes. Changes in the deposition distance can result in either spray (>10 mm) or print formation (<3 mm), with an overlap of the two in between this range. For the optimal printing distance of 0.5 mm, gradual changes in the applied voltage (0–4.5 kV) encounters transitional printing modes (dripping, micro-dripping, rapid micro-dripping, unstable and stable jetting) which can be utilised for patterning. The results indicate the robustness of the electrohydrodynamic route in the nano-materials processing arena, with emphasis on biomedical materials.

1 Introduction

Electrospraying (ES) is a well established process expanding well over a century and still being utilised heavily within a host of fields [1–3]. The process largely hinges on the formation of an electrically-induced jet, which subsequently breaks up to form fine droplets within the nano and micro range [4], depending on the processing conditions and the properties of the medium [5, 6]. The jetting mode which arises as a result of deformation, induced by the applied electrical field counteracting the medium's surface tension, can vary from a single, multi, rim and spindle - depending on the processing parameters (voltage, flow rate, distance). These modes have been studied extensively by others [2, 7].

The cone-jet mode is of particular interest, as this results in a near-uniform distribution of droplets upon jet break-up [8]. Utilisation of this mode has resulted in exuberance across the spectrum of biomedical processes, from analysis of biological molecules to the preparation of micro-capsules [9–11]. Also within the biomedical remit is tissue engineering, a rapidly growing domain which has drawn considerable interest in the processing arena. Limitations and obstacles [12, 13] posed by present methods have driven researchers to develop and expound upon existing processes to cater for growing demands for robust and efficient technologies [14, 15]. Nano-Hydroxyapatite (nHA), for example, is a ceramic mineral with applications in mainstream healthcare [16, 17], has been processed using a host of technologies such as ink-jet [18], sputter [19] and plasma coating [20]. Some of these approaches have undergone refinement [14, 21] to permit fabrication of products with possible osteological applications, demonstrated by cellular interaction. Plasma spraying, for example, is often deployed to deposit nHA on medical

Z. Ahmad (✉) · M. J. Edirisinghe · S. N. Jayasinghe ·
W. Bonfield
Department of Mechanical Engineering, University College
London, Torrington Place, London WC1E 7JE, UK
e-mail: zeeshan.ahmad@ucl.ac.uk

E. S. Thian · J. Huang · S. M. Best · W. Bonfield
Department of Materials Science and Metallurgy, University
of Cambridge, Pembroke Street, Cambridge CB2 3QZ, UK

R. A. Brooks · N. Rushton
Orthopaedic Research Unit, Addenbrooke's Hospital,
P.O. Box 180, Hills Road, Cambridge CB2 2QQ, UK

devices, and have shown to elicit positive osteological responses [22, 23]. Successful ES of this nHA, in suspension form, has been achieved to prepare sparse and dense coatings [24, 25], which have shown to elicit a favourable response towards osteoblasts in cell culturing [26, 27], signifying the viability of ES for coating biomedical materials in such manner. Preparation of scaffolds, for possible TE applications, by ES deposition on foams has also been demonstrated using advanced materials to better or enhance already existing methods [28]. Furthermore, development of a twin ES system has led to the successful synthesis of compositional variations of this material, from reagents, which highlights the presence of the preparation option within this technology [29].

From the jetting aspect of this technology, electrohydrodynamic printing (EHDP) was developed [30] and the deposition of nHA by this method has also been successfully performed [31]. Unlike the ES process, where the droplets are collected at a considerable distance from the jet break-up point, EHDP manifests by the deposition of relics or tracks very close to the break-up of the jet [32]. Thus, printing of nHA tracks (50–400 μm) has been achieved, and permitted further understanding as to how cells interact with a biomaterials surface [33]. Osteoblast response to such topographies of nHA, via EHDP, has elaborated and determined specific features of cellular response to biomaterials. Other processing technologies such as ink-jet printing and fused deposition have also been exploited to prepare structures of hydroxyapatite for biomedical evaluation [34, 35].

Two other promising off-shoots off ES technology, namely co-axial and electrospinning, also utilise jetting properties but are beyond the focus of this work.

One of the key advantages which ES systems have over other processing routes is the deployment of large nozzle diameters, when compared to other deposition methods. The nozzle diameter can easily be varied and has a direct impact on the resolution of the pattern produced [31], but this is determined by the size of the particles being processed, as blockage of the nozzle can occur, which is a common concern in several suspension processing routes. The inner diameter of the nozzle outlet is significantly larger than the end product, be it droplets forming relics or printed patterns. In other technologies, the reverse is true [36] or both the processing outlet and the end product are within close proximity of each other in terms of size.

The majority of this work is carried out on a 3D printing device [37] with an adjustable head, to permit changes in height or the *Z* axis. The board speed of the collecting substrate can also be controlled, and the processing outlet, which is a conducting nozzle, has an inner diameter of 260 μm , with an option to adjust this size. The range of inner diameters we use is 150–1,000 μm , but this can be

varied accordingly with the processing material. Here we show the ease of transition from ES to EHDP with various modes being manifest, especially during the EHDP process. The benefit of such a system is that it permits a spray and print option by adjusting the deposition height. It utilises an inner nozzle diameter much larger than the resultant deposit and the preparation of the medium is simple when compared to other methods, such as those requiring polymeric constituents [38], which have to be removed by other means. Here, we also prepare and use a simple suspension of determined wt%, composed of in-house synthesised nHA and ethanol, which evaporates rapidly upon deposition [31] with both processes; ES and EHDP, including the transitional depositions, utilising the same suspension.

Although the emphasis in this work focuses on nHA, EHD process such as EHDP and ES have been used to prepare thin ES protein films [39], ordered EHDP polymeric scaffolds and collagen [40, 41], EHDP zirconia structures [42] and ES dispersions of aspirin [43]. Therefore, the possibilities offered by EHD technology are expansive and can accommodate a variety of biomedical applications.

In this paper we show how the two processes (ES and EHDP) are linked by using a single device and a series of systematic experiments. Previous works using nHA have focused on the use of one or the other, and for EHDP have not detailed the transitions to this extent. We first show how controlled gradual changes in deposition height transfers from a spray methodology to a print methodology, so an upper limit and lower limit for either process can be established. Once the optimal printing distance is obtained, the applied voltage is gradually increased, which shows a variety of transitions, which can be used to pattern topographies. Both processes can be used to coat and pattern metallic and glass objects, and the various transitions for both processes are represented in a modified mode-selection map.

2 Experimental details

2.1 Suspension Preparation and Characterisation

The synthesis of nHA was achieved by the reaction of calcium hydroxide ($\text{Ca}(\text{OH})_2$) (AnalaR, BDH UK) with orthophosphoric acid (H_3PO_4) (AnalaR, BDH UK). 0.3 M H_3PO_4 solution was added drop-wise to 0.5 M $\text{Ca}(\text{OH})_2$ solution, while maintaining continuous stirring at ambient temperature. The pH was maintained at >10.5 by the addition of ammonia solution; hence a Ca/P ratio of 1.67 was obtained. The reaction mixture was stirred for an additional 16 h once the 0.3M H_3PO_4 solution was

completely added. The precipitate (nHA) was aged for a week, after which it was washed with boiling deionised water.

The precipitate was studied using a JOEL 200CX transmission electron microscope working at an accelerating voltage of 200 keV. The structure of nano-hydroxyapatite was also investigated using a Philips PW1730 diffractometer using $\text{CuK}\alpha$ radiation. X-ray diffraction studies were carried out at 40 kV and 40 mA with data collection from 20° – 40° with a step size of 0.05° and a scan time of 6 s.

To obtain suspensions which could be EHD processed in the cone-jet mode, the water in the suspensions was removed. This was done by gently heating the nHA precipitate until thick slurry was obtained, which was then filtered 3 times ($60\ \mu\text{m}$ pore sieve) to remove any agglomerates. To determine the new wt% of the solid fraction, samples from this slurry were taken and heated to 600°C in static air. Ethanol (BDH, UK) was added to the slurry to prepare suspensions with desired known solid fractions. Samples from this suspension were heated again to 600°C in static air to confirm the new wt% of solids. The new suspension and ethanol, which was used as a standard control and calibrating medium, were characterized for density, surface tension, pH, viscosity and electrical conductivity. Each characterisation procedure was carried out three times at ambient temperature and a mean value was taken. Viscosity was measured using a SCHOTT-viscoeasy rotational viscometer working at 100 rpm and the electrical conductivity was measured using a HANNA conductivity meter. The density was calculated using a standard density bottle (VWR, UK). The surface tension was measured using a Kruss K9 Tensiometer and the pH was measured using a standard probe (Hach-sensION).

2.2 Electrohydrodynamic deposition

The printing device was assembled by Micromech Ltd (Essex, UK). Full details of the printer design, setup and computer software used are explained elsewhere [37]. Figure 1a, b highlight the spray-print technology utilised in this work, with the difference in the deposition height between the two processes clearly visible. Figure 1c shows the difference in jetting processes and obtainable deposits are shown in Fig. 1d [31].

The desired pattern or deposition route was written and uploaded in to the form of vectors, with a two-axis framework, unlike the 3 axes we used in our 3D printing [44]. Each axis possesses $1\ \mu\text{m}$ linear encoders enabling the achievement of a few micrometers resolution. The selected design is shown in Fig. 2, with a $300\ \mu\text{m}$ allowance for print resolution. The uploaded print speed was

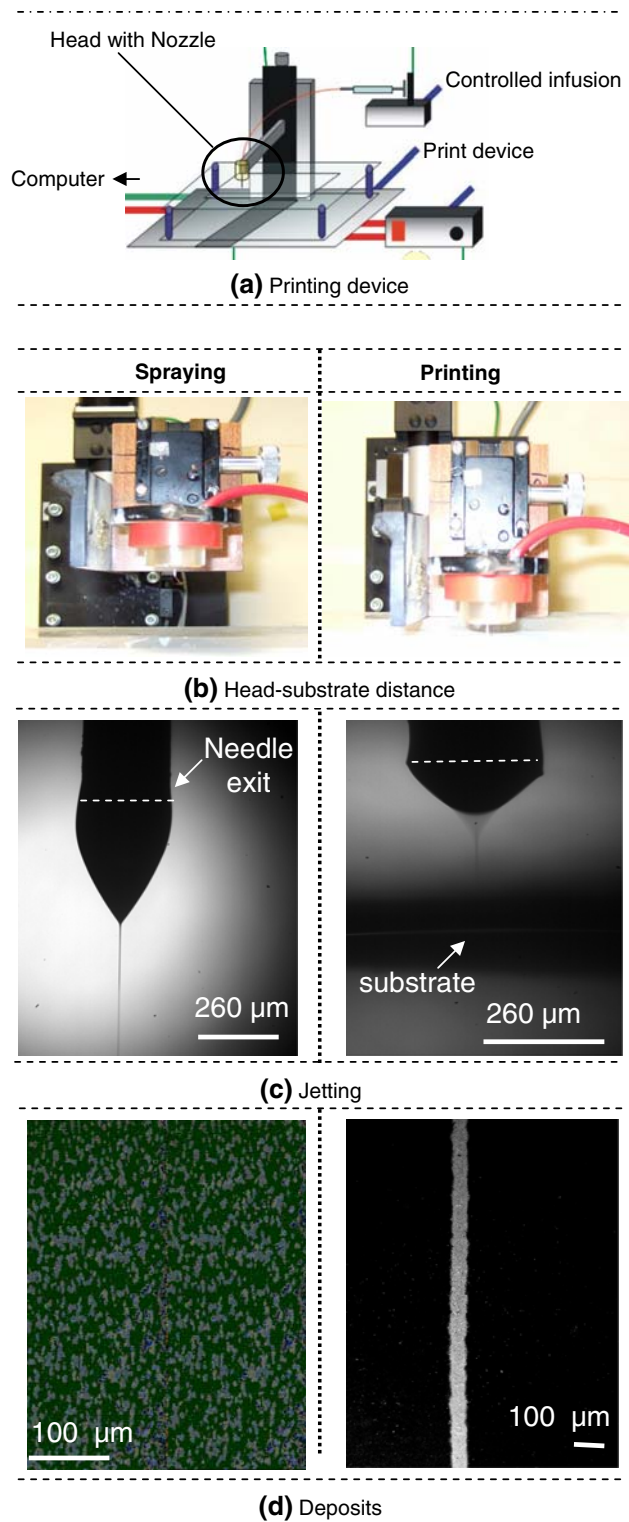


Fig. 1 Spray-print technology showing (a) illustration of printing device (b) working distance for spray and print deposition (c) jetting images during processing and (d) spray and print topographies

kept at $\sim 8\ \text{mms}^{-1}$, and is adjustable but from our previous work, this is the optimal speed. The device is operated using a programmable motion-controller–PC unit.

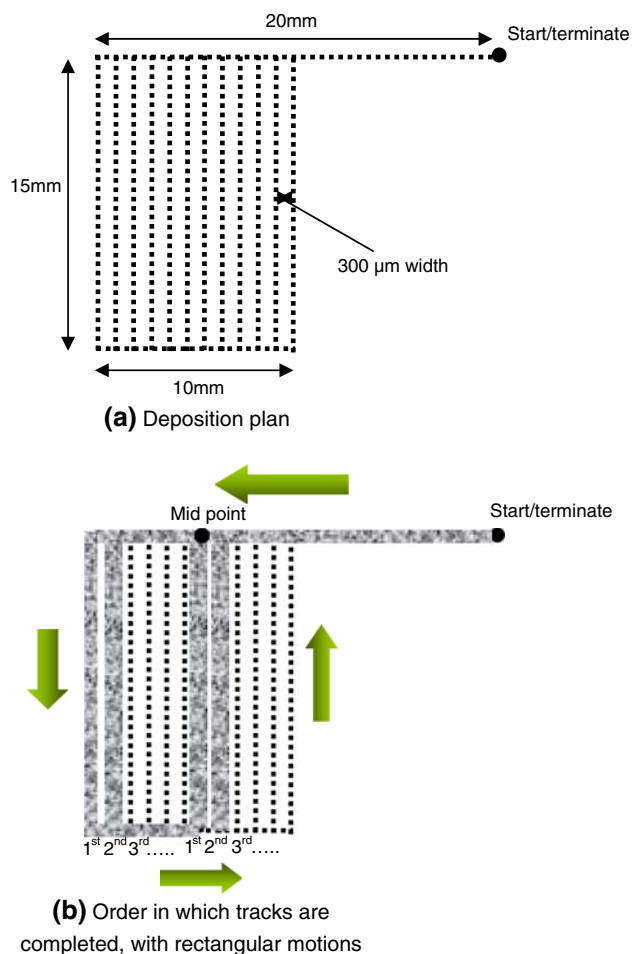


Fig. 2 Illustration showing (a) selected pattern for spray-print deposition of nHA and (b) route take by nozzle outlet

To maintain constant and continuous flow a specially designed Harvard syringe perfusor pump was used. This introduced the suspension into the 260 μm inner diameter nozzle, with silicon tubing providing the passage. The application of a voltage between the nozzle and the grounded second electrode afforded jetting. The substrates; glass slides (VWR, UK) and 2 mm stainless steel rods (GM Precision Engineering Ltd, Somerset, UK) were placed on an A4 sheet of paper which was held tightly in a purpose-built hollow perspex table frame directly below the nozzle and directly above the ground electrode. Movement in the x , y axis permit the formation of 2D structures and movement in the z axis permits the formation of 3D structures upon over-printing [31, 37]. However the z axis distance was continuously changed in one section of this work, to modify the jetting distance and no over-printing was carried out.

All samples prepared from the electrohydrodynamic processes discussed in this work were kept in the as-deposited state and there was no heat treatment. The

droplets of suspension are charged on arrival at the substrate and subsequently discharge. This should lead to better adhesion. Also, in our previous work we have observed that electrosprayed nHA deposited on titanium metal increases in adhesion after heat treatment, the nanoparticles are more clearly visible in the non-heat treated coatings and once heated the structure appears homogeneous and denser [24].

2.3 Microscopy

The printed topographies were examined by optical microscopy and then further studied using a scanning electron microscope (SEM); Hitachi SEM S3400N, operated at an accelerating voltage of 5 keV. The samples were coated with a thin layer of gold before electron microscopy.

2.4 HOB cell response to deposits: procedure and analysis

Details of both the cell culturing procedure (preparation and staining) and analysis via confocal microscopy are given elsewhere in depth [33].

3 Results and discussion

Preparation methods and quantities will have an impact on the structure of the nano-hydroxyapatite (nHA) synthesised. The nHA particles synthesised in this work are rod-shaped (Fig. 3a) with an aspect ratio of 1.5–2. The precipitate is phase pure as confirmed in the X-ray diffraction (Fig. 3b), with selected area diffraction pattern analysis showing that the material is polycrystalline (Fig. 3a).

The suspensions used for the deposition processes; print and spray, was 6.9 wt%. The properties of the suspension which influence EHD processes are shown in Table 1. A stable cone-jet mode with ethanol is more readily afforded when compared to water [45]. The electrical forces applied during the process contest with the surface tension for the jet-formation and this is largely due to the difference in surface tension of the two liquids ($20\text{--}25\text{ mNm}^{-1}$ as compared to $\sim 70\text{ mNm}^{-1}$ for water). [46]. Even with addition of nHA to ethanol, to prepare a 6.9 wt% suspension, results in a surface tension of $\sim 29\text{ mNm}^{-1}$, which is still much lower than that of water. This property favours ethanol over water for EHD processing, however it is possible to atomise water by modifying technologies which deliver lower voltages to a conducting nozzle [47].

The viscosity and electrical conductivity are perhaps the most significant properties in the outcome of the EHD process. The inclusion of 6.9 wt% nano-hydroxyapatite

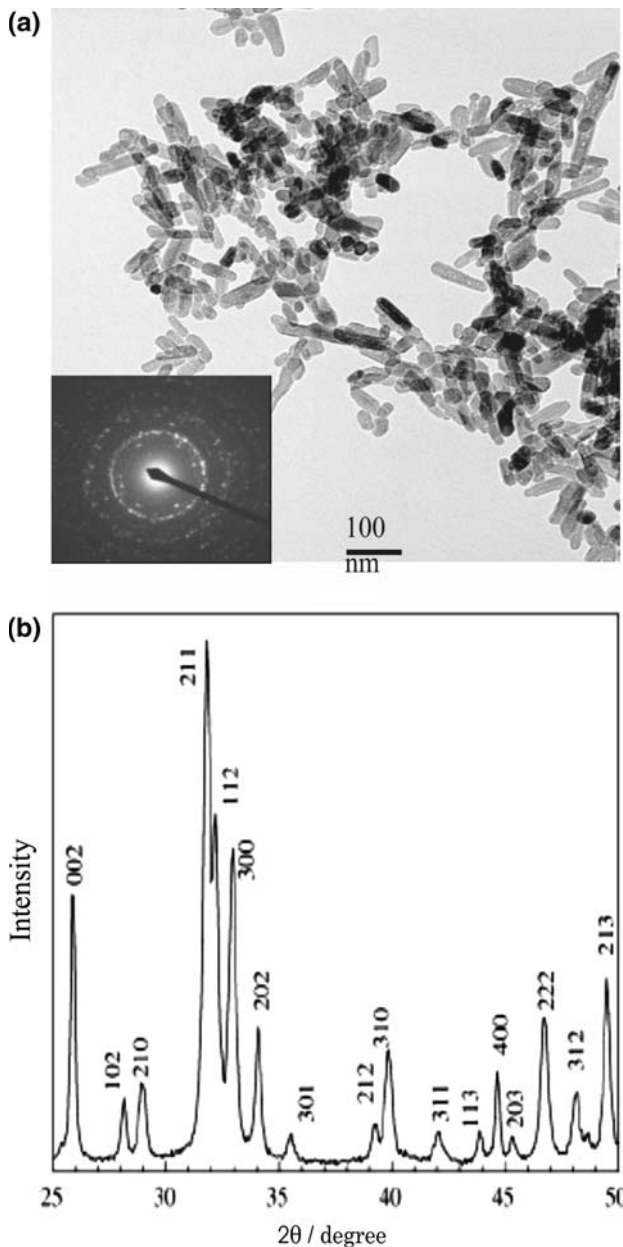


Fig. 3 Analysis of synthesised nHA particles by (a) transmission electron microscopy and (b) x-ray diffraction

Table 1 Properties of ethanol and a 6.9 wt% nano-hydroxyapatite suspension

Property	NHA suspension	Ethanol
Wt%	6.9	N/a
Density (kg m^{-3})	9.50	790
Surface tension (m Nm^{-1})	29	23
Viscosity (m Pa s)	6.8	1.3
Electrical conductivity $\text{Sm}^{-1} (\times 10^{-4})$	0.8	0.9
pH	8.2	7.2

increased the viscosity five fold with the minimal change in electrical conductivity. The former effect will give rise to larger droplets on jet break up [48].

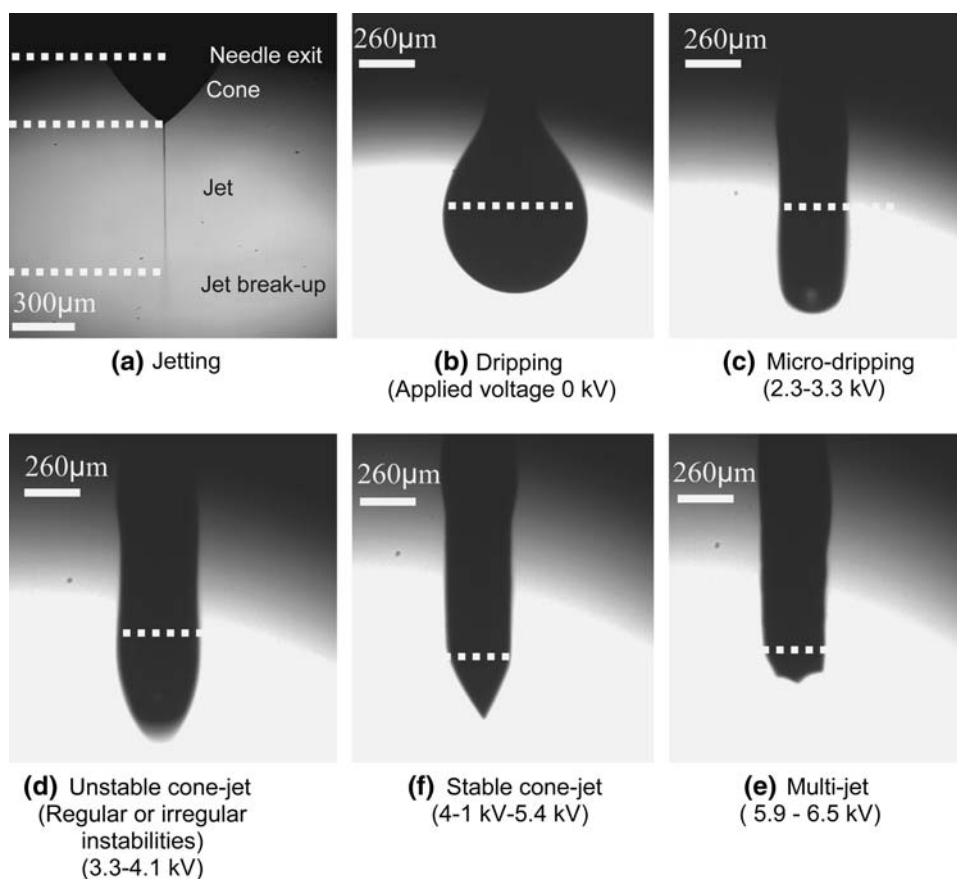
Figure 4 shows the jetting modes obtained during the application and increment of voltage to a flowing medium at fixed rate (5 $\mu\text{l}/\text{min}$) and a fixed deposition distance (15 mm). The essential features of a jet are shown Fig. 4a, namely; a cone, a jet and the jet-break up. Figure 4b shows conventional dripping, with the application of no voltage and the frequency of dripping observed to be very low, resulting in the build up of suspension around the nozzle outlet. Micro-dripping, which manifested at an applied voltage of 2.3 kV is shown in Fig. 4c, and resided until 3.3 kV, after which the unstable (3.3–4.1 kV) and stable cone-jet modes (4.1–5.4 kV) were achieved. Multi-jetting which results in a broad size distribution of drops, when compared to cone-jetting [49], was attained at 5.9 kV. Larger nozzle diameters (350–800 μm) have been used to electrospray nHA-ethanol suspensions [24] with various jetting modes appearing at different processing conditions. Such changes to the nozzle (diameter, shape or orientation) are known to have an impact on the jetting behaviour, i.e. pulsating rate [50–52].

EHDP of nHA at different flow rates is shown in Fig. 5. We have previously reported similar resolutions for prints obtained at flow rates between 1–3 $\mu\text{l}/\text{min}$ [31, 44]. Continuous printing, with reduced random instabilities, at 3 $\mu\text{l}/\text{min}$ affords prints between 100–150 μm . Preparing continuous patterns with higher resolution of $\sim 50 \mu\text{m}$ is possible at lower flow rates (1 $\mu\text{l}/\text{min}$) as shown in Fig. 5a, but at this low infusion rate, flow ceases from the nozzle due to agglomeration of particles. At higher infusion rates the resolution is reduced significantly and scatter is evident as shown in Fig. 5c–f. As the flow rate was increased, an increment to the applied voltage was required to obtain a stable cone-jet, which resulted in continuous prints.

The two processes described have been deployed to deposit materials, although EHDP is relatively new in contrast to ES. Table 2 demonstrates the ease of transition between ES and EHDP, by altering the deposition height, which ultimately alters the jetting distance. The resultant topographies from the uploaded program (Fig. 2) show significant changes to the patterning on the substrate. At a deposition distance of 20 mm, the surface of the substrate is visible, with relics (5–15 μm) clearly observable. Such relic distributions, using ES, has been used to prepare coatings and template assist coatings with possible biomedical applications [24, 53].

At a reduced deposition distance of 10 mm, the surface coating appears denser, and there is significant overlap between relics. When the distance is reduced to 5 mm, low

Fig. 4 Jetting images showing (a) jetting attributes (b) dripping (c) rapid micro-dripping (d) unstable cone-jet (e) stable cone-jet and (f) multi-jetting, all at 5 $\mu\text{l}/\text{min}$



magnification shows the presence of two faint strips on the substrate, which is due to the deposition route uploaded in the printing device. A higher magnification of the surface shows there is considerable overlap of numerous relics, but not as dense as those observed at a reduced distance of 3 mm. The desired pattern is clearly visible due to the reduced deposition distance; however, there is significant scatter between prints. At a deposition distance of 1 mm, distinct printing is observable, with reduced scatter between each track, which has a width of $\sim 300 \mu\text{m}$. The optimal distance is achieved at 0.5 mm, and this is very close to the jet break-up point. The tracks ($100\text{--}120 \mu\text{m}$) are finer and the desired pattern is obtained.

Higher resolutions are achievable [44] and with significant compromises made to the nozzle diameter sub-nanoscales resolutions have recently been achieved [54] by using pulsing modes. In this work the nozzle outlet ($260 \mu\text{m}$) was approximately double the size of printed tracks and ~ 5 times the size of relics achieved during rapid-micro-dripping for a flow rate of $3 \mu\text{l}/\text{min}$. The applied voltage at this collecting distance was varied as instabilities occur during the printing process.

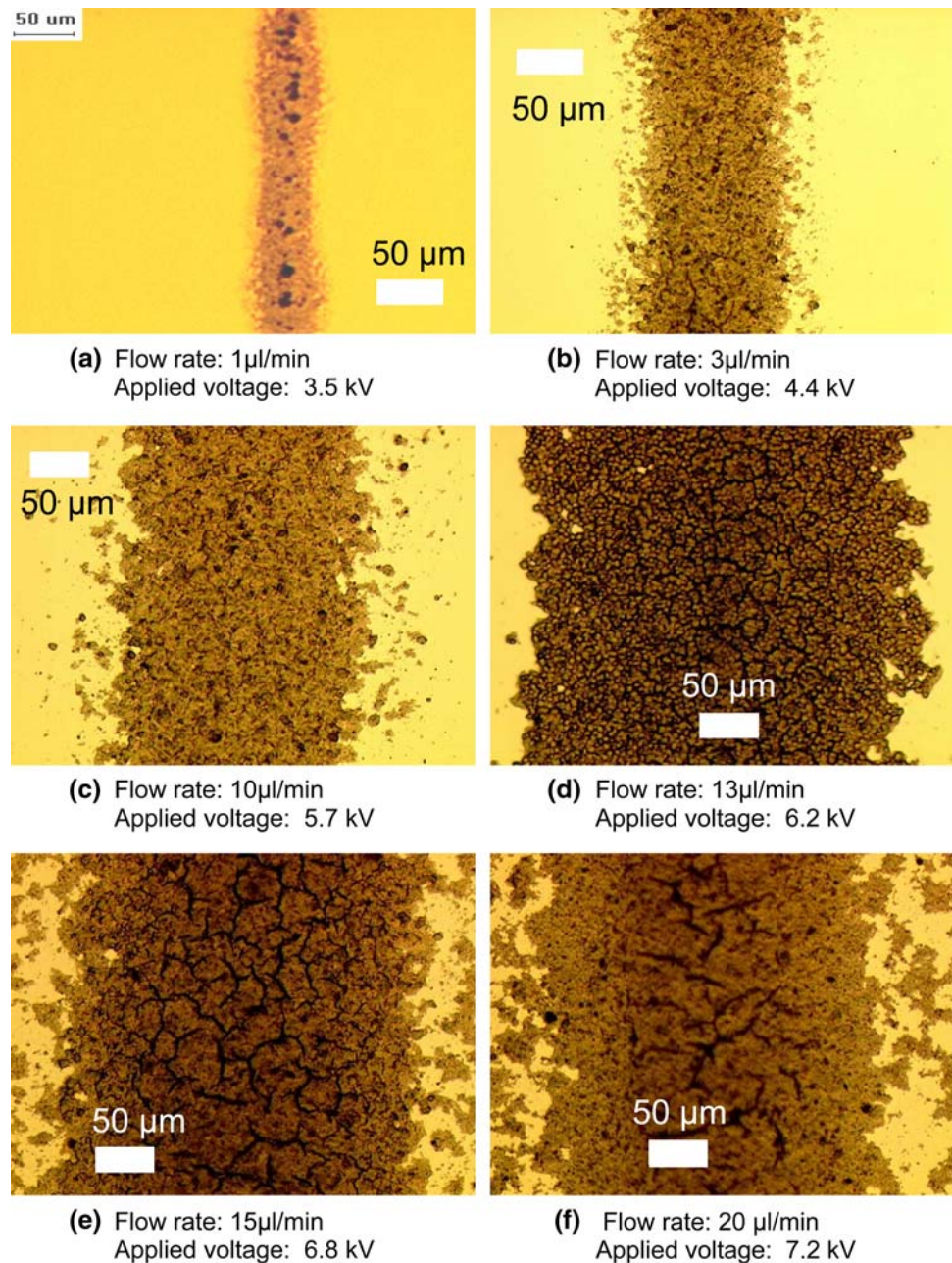
The transitions, which arise during the printing process can be assessed as a function of the applied voltage at a fixed deposition distance and flow rate. The patterning

produced across a voltage range of $0\text{--}4.5 \text{ kV}$, with a fixed flow ($3 \mu\text{l}/\text{min}$) and deposit distance (0.5 mm) is presented in Table 3.

At a deposition distance of 0.5 mm a drop generated from a dynamic force resulted in a radial feature with the diameter of $700 \mu\text{m}$, with a ring of deposit around the deposit due to the Marangoni effect [55]. Drops generated once there was significant applied voltage ($1.5\text{--}1.9 \text{ kV}$) lead to induced dripping, which caused the drops to occur more frequently, and tail on the substrate. Micro-dripping was achieved between an applied voltage of $1.8\text{--}3.2 \text{ kV}$, relics obtained during this transition were radial and had a diameter of $\sim 200 \mu\text{m}$. Within this transition, rapid micro-dripping surfaced, with relic diameters between $40\text{--}50 \mu\text{m}$. This transition has a relatively small operating window, $2.7\text{--}2.9 \text{ kV}$, when compared to the micro-dripping transition.

Unstable cone-jetting, which produced connected relic patterns, unlike the clear disconnected drops in the dripping transitions, appeared between $3.0\text{--}3.6 \text{ kV}$. This transition has been utilised by others [50] to prepare patterns, but using solutions, polymer-loaded solutions or solutions with large particulate size when compared to the nHA used in this work, where pulses were used to prepare dotted patterns for liquids down to $1\text{--}2 \mu\text{m}$, with nozzles possessing

Fig. 5 Optical micrographs for printed tracks at a flow rate ($\mu\text{l}/\text{min}$) of (a) 1 (b) 3 (c) 10 (d) 13 (e) 15 and (f) 20

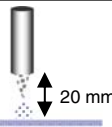
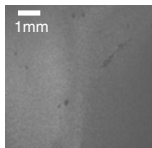
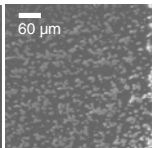
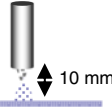
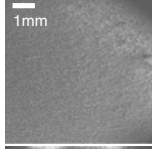
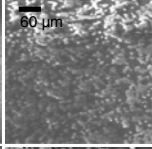
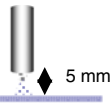
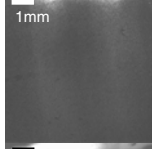
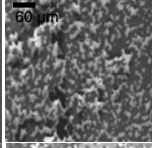
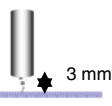
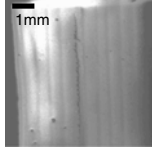
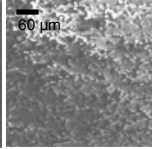
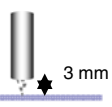
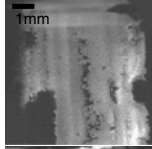
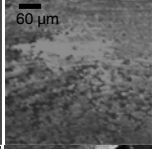
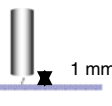
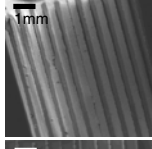
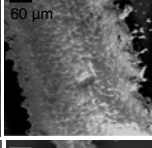
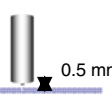
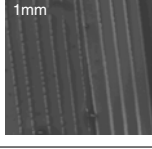
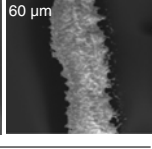


inner diameters of $\sim 50 \mu\text{m}$, but operated at slower printing speeds (1 mm/s max). These regular instabilities, coupled with the nano-sized particles in the suspension, give rise to these joined patterns during this transition, which are different to the separated drops obtained during the rapid micro-dripping and dripping processes. The prints produced at this transition had a resolution of 100–130 μm , which was significantly lower than those obtained during the rapid micro-dripping mode. This could be due to the build up of electrostatic force on both the substrate and around the operating region, all of which are within a few millimetres of each other. Beyond this voltage, the resolution is reduced and this needs to be assessed further.

The stable cone-jet mode resulted in tracks with a resolution similar to those achieved in the unstable cone-jet mode, but were attained at a higher voltage (3.4–4.3 kV). Within this voltage range the resolution can be altered, but will result in scatter, discontinuous and irregular printing, such as those shown in Table 2. Transitions occurring above stable cone-jet printing, which show increased irregular instabilities, were not assessed, although it is possible to print in a multi-jetting mode.

These transitions can be demonstrated in a modified version of a mode-selection map. Mode-selection (MS) maps [56] show various jetting modes between flow and applied voltage parameters. The MS map shown in Fig. 6

Table 2 Electrohydrodynamic deposition of nHA at different working distances, with a fixed flow rate of 3 $\mu\text{l}/\text{min}$. The working distance is defined as the gap between the nozzle exit and the collecting substrate

Distance between nozzle and substrate	Applied voltage and infused flow rate	Comment	Deposit	
			a	b
 20 mm	4.8 kV 3 $\mu\text{l}/\text{min}$	<ul style="list-style-type: none"> •Stable cone-jet •Spraying •Scattered relics visible 		
 10 mm	4.6 kV 3 $\mu\text{l}/\text{min}$	<ul style="list-style-type: none"> •Stable cone-jet •Spraying •Relic density increases 		
 5 mm	4.4 kV 3 $\mu\text{l}/\text{min}$	<ul style="list-style-type: none"> •Stable cone-jet •Spraying •Two deposited regions appear denser with respect to the overall deposit 		
 3 mm	4.3 kV 3 $\mu\text{l}/\text{min}$	<ul style="list-style-type: none"> •Stable cone-jet •Spraying. Deposition much closer to Jet break-up •Pattern clearly observable •Considerable scatter 		
 3 mm	4.2 kV 3 $\mu\text{l}/\text{min}$	<ul style="list-style-type: none"> •Unstable Jetting •Irregular spraying •Pattern clearly observable •Incomplete pattern 		
 1 mm	3.7 kV 3 $\mu\text{l}/\text{min}$	<ul style="list-style-type: none"> •Stable cone-jet •Deposition with reduced scatter, printed tracks evident •Distinct pattern 		
 0.5 mm	3.4–4.4 kV 3 $\mu\text{l}/\text{min}$	<ul style="list-style-type: none"> •Unstable and stable cone-jetting •Finer tracks printed •Deposition much closer to Jet-break-up with respect to other deposits obtained 		

shows the difference in jetting due to a change in the jetting distance and accounts for transitions observed during the EHDP and ES process. The EHDP modes were determined by deposits produced. As the deposition distance increased a greater voltage needed to be applied to enable a stable cone-jet, which also suffers less irregular instabilities at increased deposition distances. Rapid micro-dripping was only observed for the lowest deposition distance with reduced relic size when compared to micro-dripping. This may not occur in greater deposition distances as the jet break-up distance is significantly increased, when compared to the generated droplet size.

Deposits obtained from implementing ES and EHDP on steel rods are shown in Fig. 7. The deposits obtained during ES show a dense coating that was achieved over 3 min (flow rate 5 $\mu\text{l}/\text{min}$, 50 mm deposition distance, applied voltage between 5.1–5.4 kV) and was

accomplished with no disruptions to the processing method. The EHDP deposition route on metallic surfaces is far more difficult as electric discharge manifested at even low applied voltages (flow rate 3 $\mu\text{l}/\text{min}$, 2.8–3.1 kV), due to the close proximity of the metallic rod. Although hazardous, EHDP of nHA was achieved, with a track width of ~ 100 – 120 μm , however template-assisted ES of nHA has shown [53] to be more efficient than EHDP when considering patterning on metallic surfaces, largely due to using a sized template and achievable droplet sizes, highlighting the variations of EHD technologies.

One such area where patterning of nHA using these methods; via templating (ES) or direct writing methods (EHDP), is the preparation of topographies for implantable devices.

ES and EHDP forge topographies with diverse morphologies which elicit very different cellular responses.

Table 3 Electrohydrodynamic deposition at 0.5 mm with a flow rate of 3 $\mu\text{l}/\text{min}$, at varying applied voltages. FR, WD and ID refer to flow rate, working distance and inner diameter of the nozzle, respectively

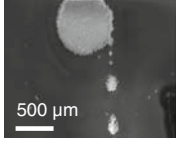
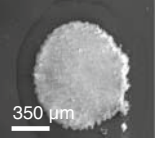
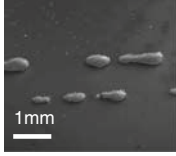
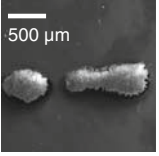
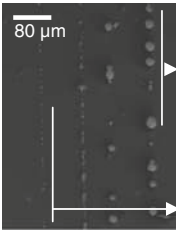
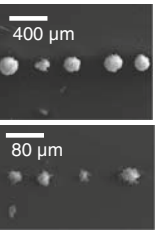
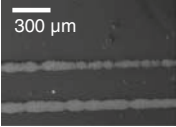
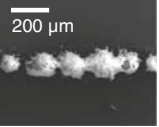
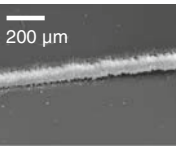
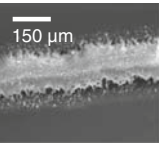
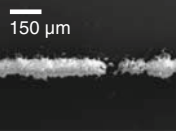
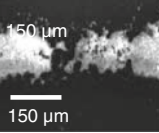
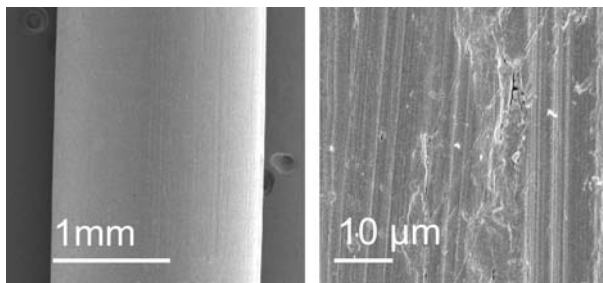
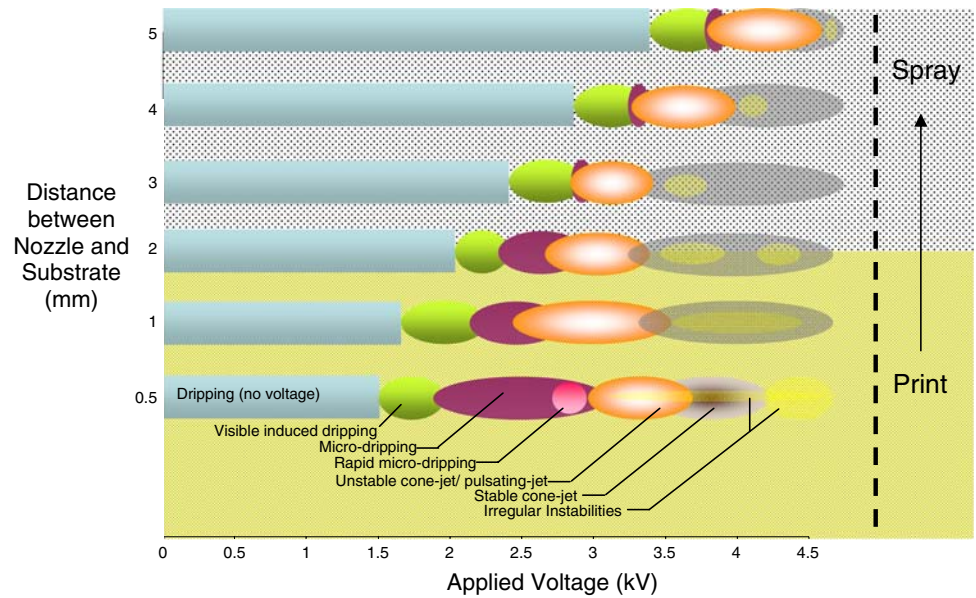
Applied voltage FR: 2 $\mu\text{l}/\text{min}$, WD = 0.5 mm ID = 260 μm	Comment	Deposit	
		a	b
0 kV 3 $\mu\text{l}/\text{min}$	<i>Dripping</i> • No Voltage • Drops 600-700 μm in size • Dripping relatively slow		
1.5-1.9 kV 3 $\mu\text{l}/\text{min}$	<i>Induced dripping (low voltage)</i> • Low applied voltage • Drop size 500-1000 μm • Drops more frequent		
1.8-3.2 kV 3 $\mu\text{l}/\text{min}$	<i>Micro-dripping and rapid micro-dripping</i> • Deposits from micro-dripping ~200 μm in size, relics separated • Deposits from rapid micro-dripping ~30-40 μm , relics separated • Applied voltage window for rapid micro-dripping is much narrower than micro-dripping.		
3.0-3.6 kV 3 $\mu\text{l}/\text{min}$	<i>Unstable cone-jet/ pulsating-jet</i> • Regular instabilities/pulsing results in drop like features which are connected. • Print resolution 100-130 μm . Higher resolution has been achieved		
3.4-4.3 kV 3 $\mu\text{l}/\text{min}$	<i>Stable cone-jet</i> • No instability to the jetting process • Processing window is narrow. • Resolution properties similar to unstable (regular) cone-jet mode.		
3.1-4.3 kV 3 $\mu\text{l}/\text{min}$	<i>Random/irregular instabilities</i> • Random breaks to tracks • Process occurs through stable and unstable jetting modes.		

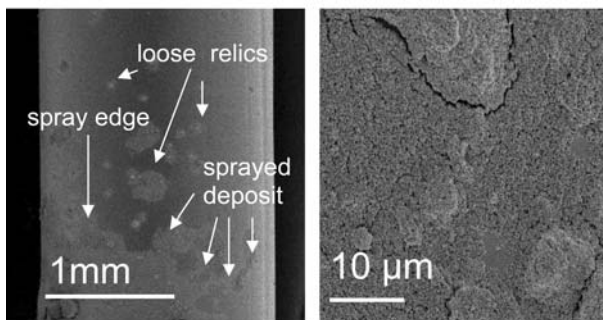
Figure 8 shows cell alignment on the two types of nHA deposited patterns, where it is clearly visible that there is a significant difference in orientation of cells and their components. Figure 8a shows cell behaviour on a deposited nHA track with a $\sim 100 \mu\text{m}$ width, obtained by EHDP, demonstrated a specific orientation for both cell bodies and cytoskeletons. Cell behaviour on an ES pattern (relics) resulted in a random orientation of cells and their components as shown in Fig. 8b.

We find that the cells align along the patterns; in addition there is also spatial interaction between cells in neighbouring patterns. These phenomena have been discussed in more detail elsewhere [57, 58]. The implications of such topographic studies deliver a better understanding into cellular behaviour at the substrate. Orthopaedic coatings can be enhanced using such methods to manipulate cell organisation, as well as influence bone integration into materials. Utilising such methods combine both the

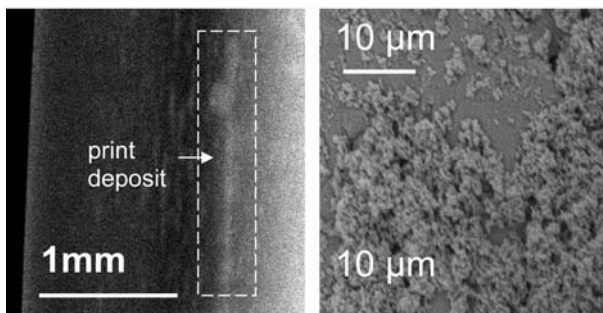
Fig. 6 Modified mode-selection map for spray-print deposition at 3 $\mu\text{l}/\text{min}$



(a) 2mm (diameter) stainless steel



(b) nHA sprayed on stainless steel rod



(c) nHA printed on stainless steel rod

Fig. 7 Stainless steel rods (2 mm diameter) with (a) no deposition (b) nHA spray deposit and (c) nHA print deposit

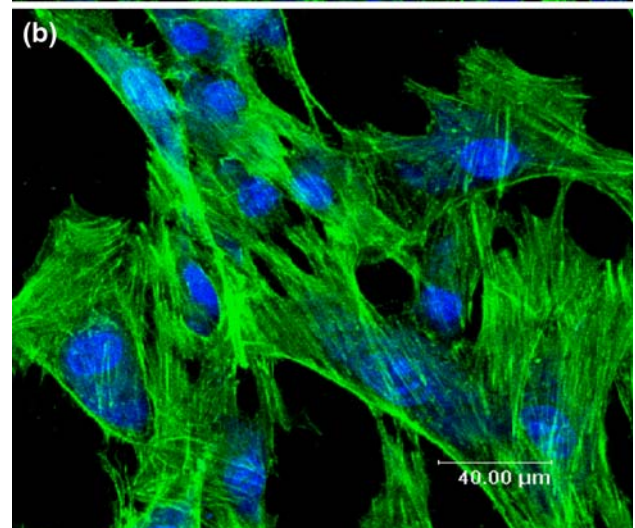
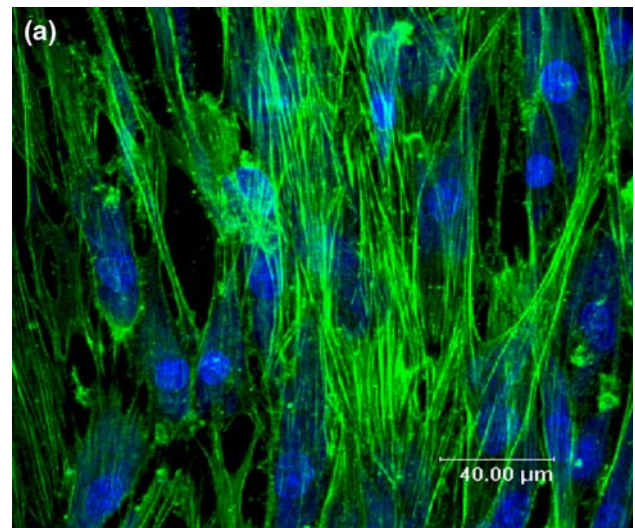


Fig. 8 Cell attachment and alignment on deposited nHA: (a) EHDP and (b) ES

chemistry and topography of materials to fabricate patterned surfaces which have in the past shown to favour certain responses which aid to strategic development of tissue engineered devices [59, 60].

4 Conclusions

Using a simple but robust EHD printing device we have shown the ease of transition between ES and EHDP for a biomedical nano-suspension. We have also elaborated on the clear transitions during the EHDP process from dripping to the stable cone-jet mode, but not beyond. Both of these interchangeable processes, ES and EHDP, were explored using a coarse nozzle, relative to other technologies in current practice, which have been used to prepare coatings and direct write patterns of biomaterials. The use of such technology is a valuable tool; providing spray, print and ease of assembling factors but more importantly comparable resolutions to existing technologies.

Acknowledgements The financial support from the UK EPSRC (Grants GR/S97880 & GR/S97873) is gratefully acknowledged. We would like to thank the Archaeology Department in UCL for the use of their microscope facilities.

References

1. A. Jaworek, A. Krupa, *J. Aerosol. Sci.* **30**, 873–893 (1999)
2. J. Zeleny, *Phys. Rev.* **3**(2), 69 (1914)
3. L. Rayleigh, *Phil. Mag.* **14**, 184 (1882)
4. A. Jaworek, *Powder Technol.* **176**(1), 18 (2007)
5. A.M. Ganan-Calvo, *Phys. Rev. Lett.* **98**(13), 134503 (2007)
6. C.E. Ho, F.G. Tseng, S.C. Lin, *J. Micromech. Microeng.* **15**(12), 2317 (2005)
7. P.D. Noymer, M. Garel, *J. Aerosol. Sci.* **31**(10), 1165 (2000)
8. R.P.A. Hartman, D.J. Brunner, K.B. Geerse, J.C.M. Marijnissen, B. Scarlett, *Electrostatics 1999 Institute of Physics Conference Series*. 163, 115
9. J.M. Fernandez, J.L.M. Vidal, P.P. Vazquez, *Chromatographia* **53**(9–10), 503 (2001)
10. S.G. Kumbar, S. Bhattacharyya, S. Sethuraman, *J. Biomed. Mater. Res. Part B* **81B**(1), 91 (2007)
11. L. Reyderman, S. Stavchansky, *Int. J. Pharm.* **124**(1), 75 (1995)
12. J.E. Lemons, *Surf. Coat. Technol.* **104**, 135 (1998)
13. J. Raghunath, J. Rollo, K.M. Sales, P.E. Butler, A.M. Seifalian, *Biotechnol. Appl. Biochem.* **46**, 73 (2007)
14. S. Limpanuphap, B. Derby, *J. Mater. Sci. Mater. Med.* **13**(12), 1163 (2002)
15. R.J. Narayan, *Int. Mater. Rev.* **51**(2), 127 (2006)
16. W. Bonfield, *Philos. Trans. R. Soc. A-Math. Phys. Eng. Sci.* **364**(1838), 227 (2006)
17. J.K.L. Burg, S. Porter, J.F. Kellam, *Biomaterials* **21**(23), 2347 (2000)
18. J.W. Halloran, *Br. Ceram. Trans.* **98**(6), 299 (1999)
19. Y.Z. Yang, K.H. Kim, J.L. Ong, *Biomaterials* **26**(3), 327 (2005)
20. H. Liang, B. Shi, A. Fairchild, *Vacuum* **73**(3–4), 317 (2004)
21. K. Van Dijk, V. Gupta, A.K. Yu, *J. Biomed. Mater. Res.* **41**(4), 624 (1998)
22. H.K. Kim, J.W. Jang, C.H. Lee, *J. Mater. Sci. Mater. Med.* **15**(7), 825 (2004)
23. J.D. Debruijn, J.S. Flach, K. Degroot, C.A. Vanblitterswijk, J.E. Davies, D.B. Jones, S.B. Doty, G. Daculsi, M.D. Mckee, *Cell. Mater.* **3**(2), 115 (1993)
24. X. Li, J. Huang, Z. Ahmad, M. Edirisinghe, *Biomed. Mater. Eng.* **17**(6), 335 (2007)
25. S.C.G. Leeuwenburgh, J.G.C. Wolke, L. Lommen, T. Pooters, J. Schoonman, J.A. Jansen, *J. Biomed. Mater. Res. Part A* **78A**(3), 558 (2006)
26. S.C.G. Leeuwenburgh, J.G.C. Wolke, T.C. Siebers, *Biomaterials* **27**(18), 3368 (2006)
27. J. Huang, S.M. Best, S.N. Jayasinghe, M.J. Edirisinghe, W. Bonfield, *Key Eng. Mater.* **284–286**, 191 (2005)
28. Q.Z. Chen, A.R. Boccaccini, H.B. Zhang, D.Z. Wang, M.J. Edirisinghe, *J. Am. Ceram. Soc.* **89**(5), 1534 (2006)
29. S.C.G. Leeuwenburgh, J.G.C. Wolke, J. Schoonman, J.A. Jansen, *Biomaterials* **25**(4), 641 (2004)
30. S.N. Jayasinghe, M.J. Edirisinghe, T. De Wilde, *Mater. Res. Innov.* **6**, 92 (2002)
31. Z. Ahmad, J. Huang, M.J. Edirisinghe, S.N. Jayasinghe, S.M. Best, W. Bonfield, R.A. Brooks, N. Rushton, *J. Biomed. Nanotechnol.* **2**, 201 (2006)
32. J.F. de la Mora, *Annu. Rev. Fluid Mech.* **39**, 217 (2007)
33. E.S. Thian, J. Huang, Z. Ahmad, M.J. Edirisinghe, S.N. Jayasinghe, D.C. Ireland, R.A. Brooks, N. Rushton, S.M. Best, W. Bonfield, *J. Biomed. Mater. Res. Part A* **85**(1), 188 (2008)
34. E. Charriere, J. Lemaitre, P. Zysset, *Biomaterials* **24**(5), 809 (2003)
35. F.C.G. De Sousa, J.R.G. Evans, *Adv. Appl. Ceram.* **104**(1), 30 (2005)
36. X. Zhao, J.R.G. Eans, M.J. Edirisinghe, J.H. Song, *Ceram. Int.* **29**, 887 (2003)
37. D.Z. Wang, S.N. Jayasinghe, M.J. Edirisinghe, *Rev. Sci. Instrum.* **76**, Art. No. 075105 (2005)
38. S. Michna, W. Wu, J.A. Lewis, *Biomaterials* **26**, 5632 (2005)
39. I. Uematsu, H. Matsumoto, K. Morota, *J. Colloid Interface Sci.* **269**(2), 336 (2004)
40. A. Gupta, A. Seifalian, Z. Ahmad, M. Edirisinghe, M. Winslet, *J. Bioact. Compat. Polym.* **22**, 265 (2007)
41. H.S. Kim, D.Y. Lee, J.H. Park, J.H. Kim, J.H. Hwang, H.I. Jung, *Exp. Tech.* **31**(4), 15 (2007)
42. D.Z. Wang, S.N. Jayasinghe, M.J. Edirisinghe, *J. Nanopart. Res.* **7**, 301 (2005)
43. S.W. Li, S.N. Jayasinghe, M.J. Edirisinghe, *Chem. Eng. Sci.* **61**(10), 3091 (2006)
44. Z. Ahmad, J. Huang, E.S. Thian, M.J. Edirisinghe, S.N. Jayasinghe, S.M. Best, W. Bonfield, R.A. Brooks, N. Rushton, *J. Biomed. Nanotechnol.* (accepted and in press)
45. G.M.H. Meesters, P.H.W. Vercoulen, J.C.M. Marijnissen, *J. Aerosol. Sci.* **23**, 37 (1992)
46. O.V. Salata, *Curr. Nanosci.* **1**(1), 25 (2005)
47. O. Lastow, W. Balachandran, *J. Electrostat.* **65**(8), 490 (2007)
48. S.N. Jayasinghe, M.J. Edirisinghe, *J. Aerosol. Sci.* **33**(10), 1379 (2002)
49. O. Wilhelm, L. Madler, *Atomization and Sprays*. **16**(1), 83 (2006)
50. M.D. Paine, M.S. Alexander, K.L. Smith, *J. Aerosol. Sci.* **38**(3), 315 (2007)
51. J.P. Borra, Y. Tombette, P. Ehouarn, *J. Aerosol. Sci.* **30**(7), 913 (1999)
52. C.H. Chen, M.H.J. Emond, E.M. Kelder, B. Meester, J. Schoonman, *J. Aerosol. Sci.* **30**(7), 959 (1999)
53. X. Li, J. Huang, M.J. Edirisinghe, *J. R. Soc. Interface* **5**(19), 253 (2008)
54. J. Park, M. Hardy, S.J. Kang, K. Barton, K. Adair, D.K. Mukhopadhyay, C.Y. Lee, M. Strano, A.G. Alleyne, J.G. Georgiadis, P.M. Ferreira, J.A. Rogers, *Nature Materials*. **6**, 782 (2007)

55. R.D. Deegan, O. Bakajin, T.F. Dupont, G. Huber, S.R. Nagel, T.A. Witten, *Nature*. **389**(23), 827 (1997)
56. S.N. Jayasinghe, M.J. Edirisinghe, *Appl. Phys. A Mater. Sci. Process.* **80**(2), 399 (2005)
57. E.S. Thian, Z. Ahmad, J. Huang, M.J. Edirisinghe, S.N. Jayasinghe, D.C. Ireland, R.A. Brooks, N. Rushton, W. Bonfield, S.M. Best, *J. Bionanoscience*. **1**(1), 60 (2007)
58. E.S. Thian, Z. Ahmad, J. Huang, M.J. edirisinghe, S.N. Jayasinghe, D.C. Ireland, R.A. brooks, N. Rushton, W.Bonfield, S.M. Best, *Biomaterials* **29**(12), 1833 (2008)
59. D. Perizzolo, W.R. Lacefield, D.M. Brunette, *J. Biomed. Mater. Res.* **56**, 494 (2001)
60. S.N. Bhatia, M.L. Yarmush, M. Toner, *J Biomed Mater Res.* **34**, 189 (1997)